Biophysical Journal Volume 102 February 2012 587–596


# Effect of Sequence Variation on the Mechanical Response of Amyloid Fibrils Probed by Steered Molecular Dynamics Simulation

Hlengisizwe Ndlovu,[†‡] Alison E. Ashcroft,[‡§] Sheena E. Radford,[‡§] and Sarah A. Harris[†‡*]
[†]School of Physics and Astronomy, [‡]Astbury Centre for Structural Molecular Biology, and [§]Institute of Molecular and Cellular Biology, University of Leeds, Leeds, United Kingdom

ABSTRACT The mechanical failure of mature amyloid fibers produces fragments that act as seeds for the growth of new fibrils. Fragmentation may also be correlated with cytotoxicity. We have used steered atomistic molecular dynamics simulations to study the mechanical failure of fibrils formed by the amyloidogenic fragment of human amylin hIAPP20-29 subjected to force applied in a variety of directions. By introducing systematic variations to this peptide sequence in silico, we have also investigated the role of the amino-acid sequence in determining the mechanical stability of amyloid fibrils. Our calculations show that the force required to induce mechanical failure depends on the direction of the applied stress and upon the degree of structural order present in the $\beta$-sheet assemblies, which in turn depends on the peptide sequence. The results have implications for the importance of sequence-dependent mechanical properties on seeding the growth of new fibrils and the role of breakage events in cytotoxicity.

## INTRODUCTION

Amyloid fibrils are formed when peptides or misfolded proteins self-assemble into filamentous aggregates. They are associated with a number of neurodegenerative and pathological human diseases such as Alzheimer's, Parkinson's, and type II diabetes (1). It is still not clear, however, if the fibrils are the cause or merely symptomatic by-products of the disease (2). Although some studies have shown that the oligomeric structures arising during the early stages of fibril formation are toxic (2–4), other studies indicate that the mature fibrils are also toxic agents (5–7). Moreover, the brittleness of amyloid fibrils also influences aggregation and toxicity. In yeast prions, the fragmentation of mature fibrils has been shown to increase fibril load through seeding by increasing the number of ends from which new fibrils may grow (8,9). The fragility of these fibrils also dictates the strength and penetrance of the strain phenotype in different yeast species (8).

Experimental work using a range of fibril species, including $\beta$2-microglobulin and $\alpha$-synuclein, has highlighted a connection between the fragmentation of mature fibrils and an increase in their toxic properties (10,11). In these studies, reducing the fibril length through mechanical agitation made the fibrils more disruptive to liposome membranes and more cytotoxic to the cell lines studied. Another study using two conformationally distinct polymorphs of the Syrian hamster prion protein showed the fibril fragments were indeed more toxic for one state but that the fragments of the other state were substantially less toxic than the intact fibrils (5). A firm understanding of the structural factors that influence the mechanical brittleness of fibrils, the choreography of breakage events, and the molecular details of the fragments remaining after mechanical failure could aid in the interpretation of seeding and toxicity experiments and ultimately provide a basis for the design of therapeutic agents to combat amyloid disease.

Despite the biomedical importance of the mechanical properties of amyloid fibrils, few biophysical techniques are available that are able to characterize their response to force experimentally at the molecular level. This is due in part to practical limitations on how the fibrils can be prepared and tethered while the deformation is applied. Atomic force microscopy (AFM) has been used to mechanically probe an adhesive secreted by a marine invertebrate (*Entobdella soleae*) (12,13) that contains mechanically functional amyloid. The AFM technique has also been used to measure the elastic modulus of a number of amyloid and amyloidlike fibril species through force spectroscopy and nanoindentation (14–18) experiments that measure the local response of a selected region rather than that of the fibril as a whole.

Analysis of AFM topographic data taken from images of a number of fibril species, to obtain their bending rigidity, reveals that fibrils have a high elastic modulus whose molecular basis stems from backbone intermolecular hydrogen bonding (19). Synchrotron x-ray diffraction at high pressures has been used to study fibrils under mechanical compression (20) and reproduces elastic moduli comparable to AFM experiments. Computer simulations, in which the geometry of the system being studied and the manner in which force is applied can be precisely controlled,

*Submitted September 9, 2011, and accepted for publication December 9, 2011.*

*Correspondence: s.a.harris@leeds.ac.uk



Editor: Nathan Baker.


0006-3495/12/02/0587/10

doi: 10.1016/j.bpj.2011.12.047

are particularly valuable in complementing experimental studies. Steered molecular dynamics (SMD) simulations have been used to probe the force-induced unbinding of a single peptide from A$\beta$ fibrils (21) and demonstrated an anisotropic response relative to the pulling direction. Computer simulations have also been used to measure the Young's modulus of A$\beta$ fibrils (22). These simulations probed the fibrils' response to compressive loading and their failure under tensile loading conditions (22–24).

In this work, atomistic SMD has been used to apply sufficient mechanical stress to induce mechanical failure, during which fibrils formed by the wild-type and a series of variants of the amyloidogenic region of human amylin hIAPP20-29 are forced to fragment into two or more aggregates that are then separated by intervening solvent molecules. Four deformation protocols that apply force in a defined direction were chosen so as to interrogate either the stabilizing hydrophobic core interactions between a pair of $\beta$-sheets or the hydrogen-bond network within each $\beta$-sheet. A schematic representation of the four schemes (peel, stretch, slide, and shear) is provided in Fig. 1. Peel involves pulling the pair of stacked $\beta$-sheets apart, whereas stretch elongates the fibril along its length until it reaches its tensile limit. Shear applies forces perpendicular to the length of the fibril by pulling atoms along the axis of the peptide strands. Finally, the slide deformation drags one entire $\beta$-sheet across another with the pulling direction parallel to the fibril long axis.

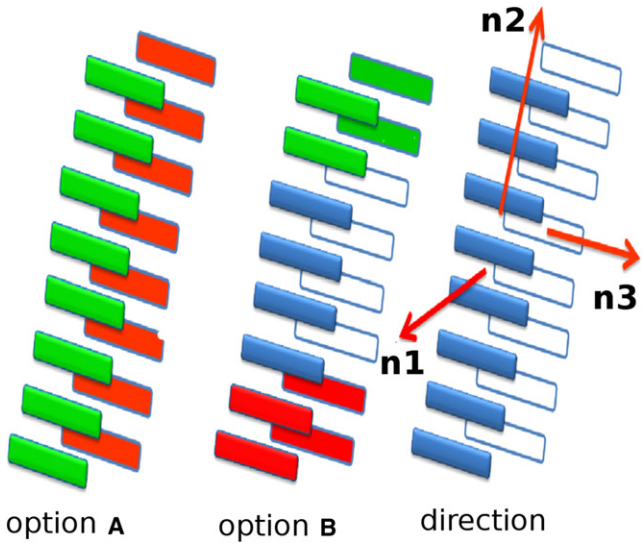


FIGURE 1 (*Color available online only.*) Schematic representation of the deformations applied to fibril models. Each deformation is defined by pulled/fixed atom choice (either *A* or *B*) and then a pulling direction (*n*1, *n*2, or *n*3). (*Green*) Peptides whose backbone C$\alpha$ atoms are pulled. (*Red*) Peptides with C$\alpha$ atoms held fixed. All other atoms in these peptides are free to move. Peel deformation: option *A* and *n*1. Stretch deformation: option *B* and *n*2. Slide deformation: option *A* and *n*2. Shear deformation: option *B* and *n*3.

In addition to comparing the mechanical properties of fibrils subjected to force applied in a variety of directions, we have also investigated the role played by the amino-acid sequence in the mechanical stability of amyloid fibrils. Model fibrils were built from the amyloidogenic fragment of human amylin SNNFGAILSS peptide sequence based on structural information on the parallel $\beta$-sheet polymorph available from solid-state (ss) NMR (25). This sequence and its derivatives have been widely used in both experimental (26–31) and computational studies (32–35) of amyloid-related phenomena. We then designed a series of peptide sequences in which an increasing proportion of residues are substituted with those present in the nonamyloidogenic rat amylin counterpart (see Table 1). The rat sequence acts as a control for the SMD simulations because it is not able to form stable amyloid fibrils in vitro (26). The variants were chosen so that none of the amino-acid substitutions removes or adds a residue that is a potential donor or acceptor of side-chain hydrogen bonds. The first three and last two residues of hIAPP were therefore not changed (except in rat-IAPP), as these residues (Ser and Asn) can potentially participate in side-chain hydrogen bonding. Model fibrils for this series of new sequences were constructed in silico by substituting the appropriate residues in the wild-type ssNMR structure.

## MATERIALS AND METHODS

A more detailed description of the methods used is provided as the Supporting Material.

### Construction of the fibril models

The initial fibril model was built from coordinate files derived from solid state NMR data for the parallel polymorph of SNNFGAILSS fibril (25) using the Nucleic Acid Builder software package (36). The model fibril consisted of a pair of $\beta$-sheets, each containing eight peptides (an $8 \times 2$ fibril model). The peptide sequence of the $8 \times 2$ model was altered (see the Supporting Material) to produce six distinct fibril variants, each of which contain one or more amino acids from the nonamyloidogenic rIAPP sequence. The relevant substitution was applied to all 16 peptides in the pair of $\beta$-sheets. The naming convention adopted for these substitutions arise from numbering the amino-acid residues of the SNNFGAILSS sequence from 1 to 10, and are provided in Table 1. For example, the F4L variant relates to a substitution of Phe in the fourth position with a Leu residue.

**TABLE 1 Models built from substitutions of amino acids from the original hIAPP$_{20-29}$ sequence**

| Model | Peptide sequence |
|---|---|
| Wild-type (hIAPP) | $NH_2$- SNNFGAILSS-COOH |
| F4L | $NH_2$- SNN<u>L</u>GAILSS-COOH |
| A6P | $NH_2$- SNNFG<u>P</u>ILSS-COOH |
| I7V | $NH_2$- SNNFGA<u>V</u>LSS-COOH |
| F4L-A6P | $NH_2$- SNN<u>L</u>G<u>P</u>ILSS-COOH |
| F4L-A6P-I7V | $NH_2$- SNN<u>L</u>G<u>P</u><u>V</u>LSS-COOH |
| Rat-IAPP | $NH_2$- SNN<u>L</u>G<u>P</u><u>V</u>L<u>P</u><u>P</u>-COOH |

Specific changes are underlined.

## Molecular dynamics simulations

MD simulations were run in both the AMBER9 (37) and NAMD2.7b1 (38) software packages, with the all-atom AMBER99SB (39) and the CHARMM22/CMAP (40) force fields, respectively. The 8 × 2 ssNMR model and the associated fibril variants were explicitly solvated in a periodic water box of TIP3P (41) molecules. The fibrillar assemblies were subjected to careful equilibration before the unrestrained production run of 22-ns MD for each fibril model. All MD was run at constant temperature (300 K) and pressure (1 atm). Convergence was monitored using the root mean-square deviation and was sufficient for all models within the final 6 ns of 22-ns MD (see Fig. S1 in the Supporting Material). To check that these conformations were force-field-independent, the simulations were rerun in NAMD using the CHARMM22/CMAP force field. No significant structural changes were observed after 10 ns of these validation simulations.

## Steered molecular dynamics

Conformations of the fibrils from the end of the unrestrained MD simulations served as initial structures for steered molecular dynamics (SMD) simulations to characterize mechanical stability. SMD was performed using the NAMD2.7b1 package (38) and the CHARMM22/CMAP force field (40). The deformations (peel, stretch, shear, and slide) consisted of forcing a defined set of atoms to move (using a spring constant of 500 pN/Å) at a constant pulling velocity (0.01 Å/ps) while another group of atoms was fixed (Fig. 1). All other atoms are free to move during the simulations. SMD was performed for 4 ns, except for the peel simulations that were only 2 ns, due to the smaller displacements required for this deformation mode. Each SMD simulation was repeated four times, with randomized starting velocities to ensure the trajectories sampled different areas of phase space. Additional simulations to check the dependence of mechanical response on the choice of force field were carried out using the AMBER99SB force field. The trends recorded in the simulations using the CHARMM22/CMAP and AMBER99SB force fields were similar (see Fig. S2 *a*). A series of peel simulations was also performed at different pulling velocities (0.5, 0.1, 0.05, 0.01, and 0.001 Å/ps), which demonstrated that the trends in peak force with sequence are not unique to the pulling velocity chosen (see Fig. S2 *b*) during this deformation.

## Analysis methods and calculations

Analysis of the unrestrained MD simulations was performed on snapshots sampled every 1 ps from the final 6 ns of the MD trajectory. Secondary structure content was monitored using the DSSP method (42) via the PTRAJ module in the AMBER 9 package (37). The HBONDS utility available in VMD (43) was used to analyze the occupancies of the backbone and side-chain interstrand hydrogen bonds. The MM-PBSA methodology as implemented in AMBER11 (37) was used to calculate enthalpies of the fibril models stripped of solvent molecules. Noise reduction in force-time profiles was achieved with a moving median filter (see Fig. S3).

# RESULTS

## Effect of sequence substitution on fibril conformation

To examine the effect of the sequence substitutions on fibril structure and energetic stability, models of fibers containing two $\beta$-sheets, each comprised of eight $\beta$-strands in a parallel organization, were constructed in silico. Unrestrained MD simulation was run for 22 ns on the model fibrils constructed from the wild-type (based on ssNMR structures of SNNFGAILSS (25)) and each of the related sequence variants, and the final 6 ns subjected to analysis. The resulting structures (Fig. 2) showed effects that ranged from subtle changes to drastic reductions in the degree of order in the aggregates relative to the wild-type model. To quantify the degree of order within the fibrils, the mean fraction of secondary structure elements present during the course of the dynamics was computed and is shown in Fig. 3 *a*. The mean occupancies of interstrand backbone hydrogen bonds and side-chain hydrogen bonds are shown in Fig. 3 *b*. The calculated energetic stabilities of the variant models relative to the wild-type fibrils are shown in Fig. 3 *c*. The individual energy terms contributing to the enthalpy are listed in Table S1 in the Supporting Material for each fibril model.

Of the single point changes, the substitution of phenylalanine for leucine at position 4 (F4L) results in a model fibril that is most similar to that formed by the wild-type sequence after MD, because the proportion of $\beta$-strands and number of backbone and side-chain hydrogen bonds is identical (within error) in the two fibril models (Fig. 3, *a* and *b*). This observation is consistent with experimental data from electron microscopy (EM) and transmission electron microscopy images, which show that fibril aggregates

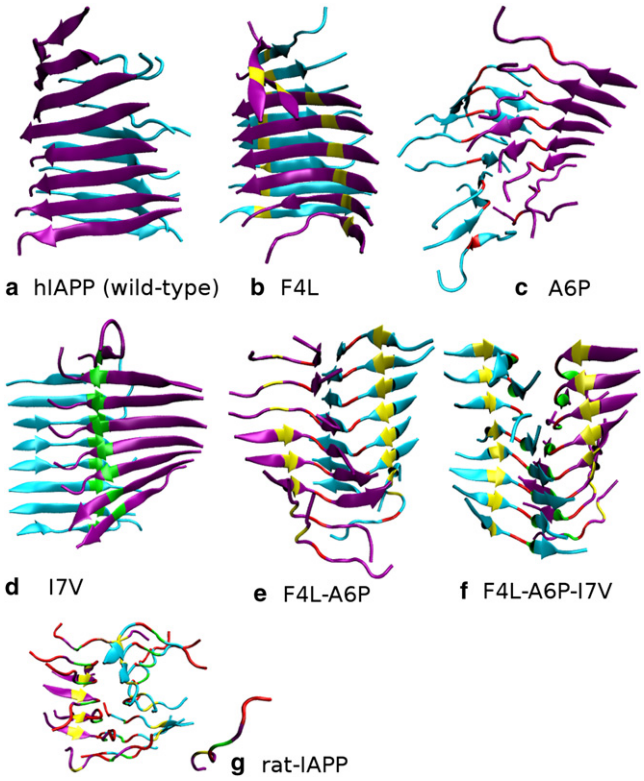


FIGURE 2 (*Color available online only.*) Final configurations of the fibrils at the end of the (22 ns) MD simulations performed in the absence of force. (*a*) Wild-type model with sequence SNNFGAILSS, (*b*) variant with F4 substituted with leucine (marked in *yellow*), (*c*) variant with A6 substituted with proline (marked in *red*), (*d*) variant with I7 substituted with valine (marked in *green*), (*e*) double substitution F4L/A6P, (*f*) triple substitution A6P/F4L/A6P, and (*g*) the nonamyloidogenic rat amylin fragment SNNLGPVLPP.

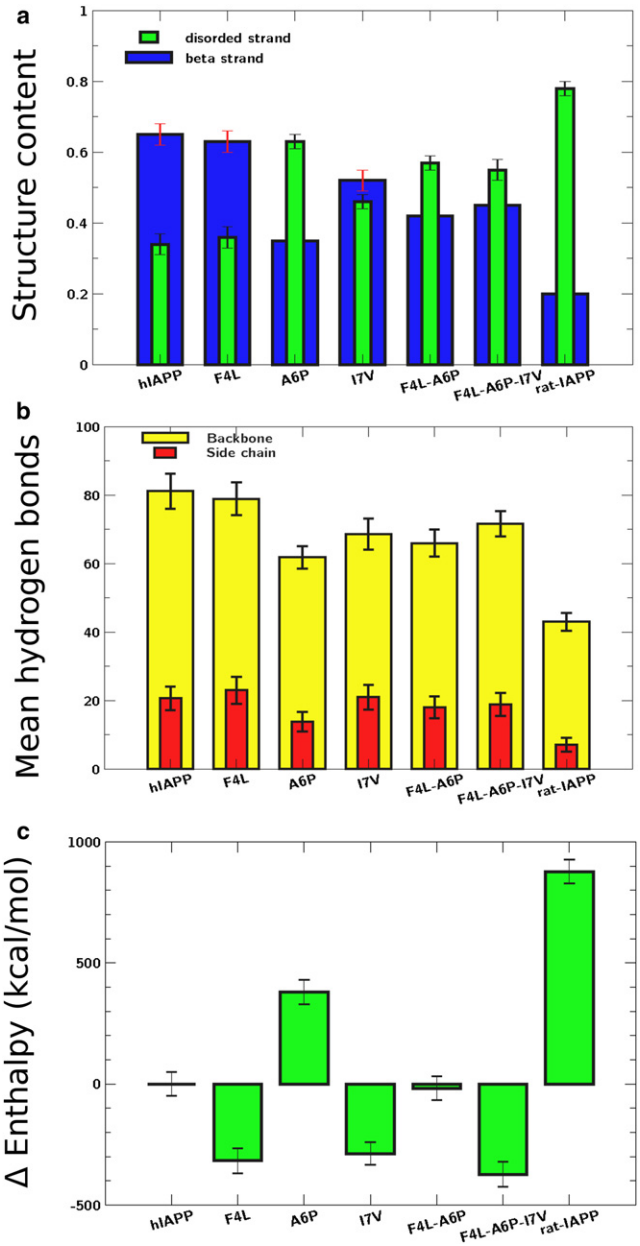


FIGURE 3 (*Color available online only.*) (*a*) Mean fraction of secondary structure elements present in each fibril model from 1-ps snapshots of the final 6 ns of MD simulation. (*Blue*) $\beta$-strand content. (*Green*) Random coils. (*b*) Mean number of interstrand backbone (*yellow*) and side-chain (*red*) hydrogen bonds recorded in the final 6 ns of MD. (*c*) The configurational enthalpy plotted relative to the wild-type fibril model.

form readily from the F4L variant, giving rise to fibrils that are morphologically identical to those formed from the wild-type peptide (26,30). EM images obtained by Westermark et al. (26) of fibrils formed from the isoleucine-to-valine (I7V) variant show that the fibril bundles also have a similar morphology to those formed from the wild-type peptide. During the MD, the substitution of isoleucine for valine (I7V) results in a shift of one $\beta$-sheet relative to the other, with the N-terminal regions on the opposing sheets becoming more solvent-exposed than in the wild-type fibrils. Nevertheless, the aggregates remain ordered, with only a 15% and 20% decrease in hydrogen bonding and $\beta$-sheet content, respectively (Fig. 3, *a* and *b*), and no measurable change in the number of side-chain hydrogen bonds.

Both the F4L and I7V fibrils are more energetically stable than the wild-type fibril model (Fig. 3 *c*). In contrast, the introduction of a proline residue in place of alanine (A6P) disrupts the fibril structure and results in an increase of random coiled regions at the expense of the $\beta$-strand motif (Fig. 3 *a*), reduced side-chain hydrogen bonding (Fig. 3 *b*), a reduced energetic stability relative to the wild-type (Fig. 3 *c*), and aggregates that are visibly disordered (Fig. 2). The EM images from Westermark et al. (26) of fibrils formed by the A6P variant show that fibrils formed from this sequence are morphologically distinct from those formed from the wild-type peptide. The double (F4L-A6P) and the triple (F4L-A6P-I7V) substitutions give rise to fibrils that share similar secondary structure characteristics to each other; A6P-I7V possessed more (72 $\pm$ 4 compared with 66 $\pm$ 4) interstrand backbone hydrogen bonds at the end of MD, but there were no detectable differences in side-chain hydrogen-bonding interactions between the two variants. The fibril model mimicking the nonamyloidogenic rat sequence, SNNLGPVLPP, which contains three proline residues, showed a dramatic transition from its initial ordered configuration into an amorphous globularlike aggregate of random coils (Figs. 2 *g* and 3 *a*). There is also a significant reduction in the energetic stability relative to its wild-type counterpart (Fig. 3 *c*) by the end of the MD simulation. This is consistent with experimental studies that show that this sequence is unable to form stable amyloid fibrils (26). In the SMD simulations described below, this amorphous aggregate serves as the reference state for quantifying the mechanical resistance of ordered fibril models.

## The mechanical strength of fibrils depends on the type of deformation applied and on sequence

To characterize the different mechanical resistances of model fibrils formed from the wild-type fragment of hIAPP and its six variants, structures taken from the end of the initial MD simulations were each subjected to four equivalent SMD simulations in each of the four deformation directions shown in Fig. 1 (112 SMD simulations in total). Fig. 4, *a–d*, shows a selection of representative configurations of the fibrils sampled from the peel, stretch, slide, and shear SMD simulations. The relevant force-time profile is plotted alongside for one of the four repeat simulations. Fig. S4 in the Supporting Material shows the force-time profiles measured for the wild-type fibril models in the four pulling directions. Although each repeat SMD simulation follows a slightly different path through conformational space, similar features are observed in all equivalent

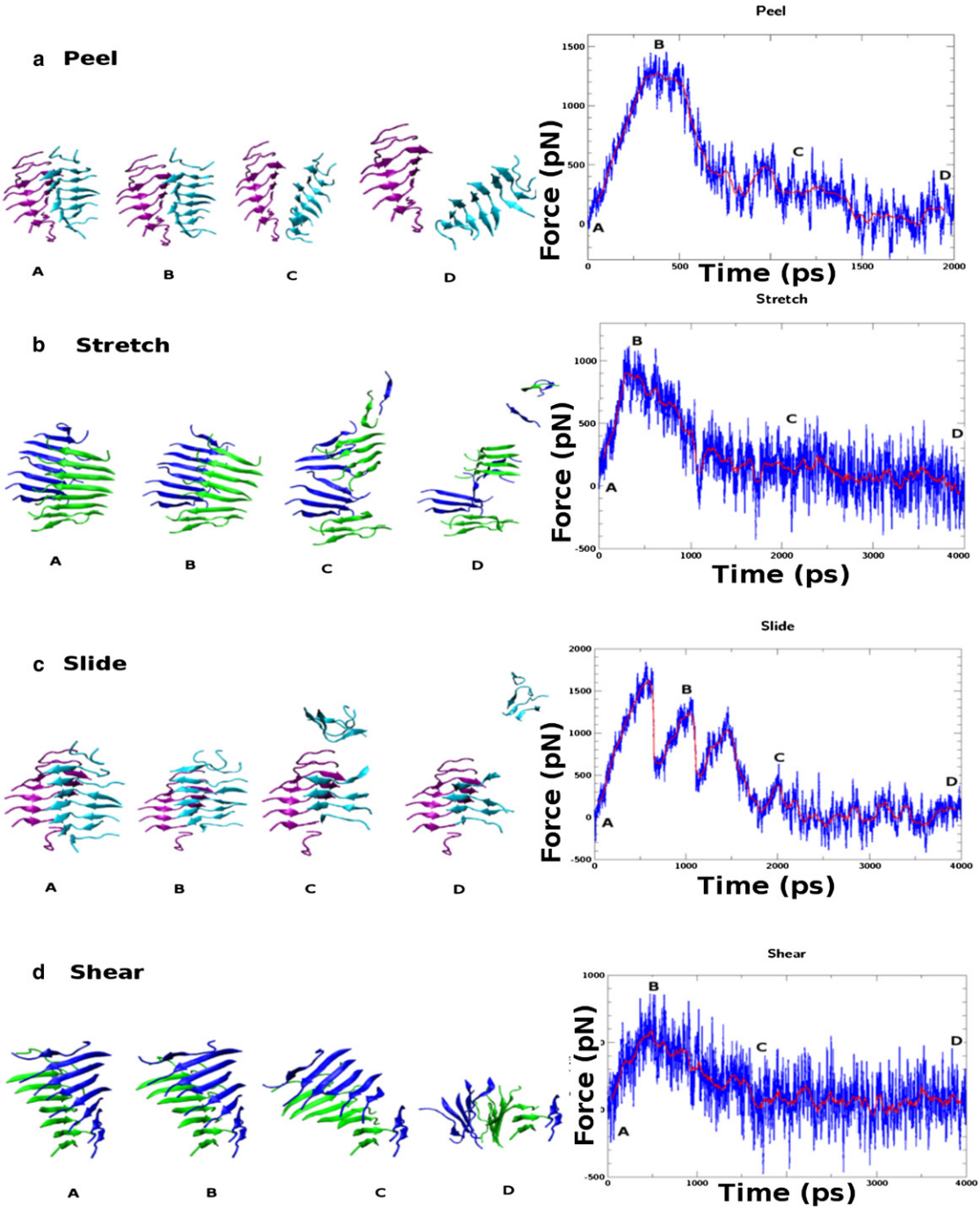


FIGURE 4 (*Color available online only.*) Representative snapshots of the fibrils evolving in time as the different deformation protocols are applied. (*Right side* of each *snapshot sequence*) Relevant force-time profile is plotted. (*Solid red line*) Filtered signal from which the peak force is measured. (*a*) Peel, F4L-A6P trajectory. (*b*) Stretch, I7V trajectory. (*c*) Slide, F4L-A6P trajectory. (*d*) Shear, wild-type fibril trajectory.

force-time profiles. The force profiles for the six variant fibrils are shown in Fig. S5, Fig. S6, Fig. S7, and Fig. S8.

The magnitude of the average peak force calculated over the four repeat simulations was used as a measure of the mechanical resistance of the fibril to deformation along a particular direction. The peak force is defined as the maximum force exerted during a given SMD simulation after the data have been filtered to reduce thermal noise (see the Supporting Material). For the rat amylin sequence (rIAPP20-29), which collapses during the equilibration phase into a disordered aggregate, some of the SMD protocols (such as sliding sheets past each other) become ambiguous and difficult to implement. In these cases, all four deformation simulations were carried out for the rIAPP

variant using atom selections consistent with those used for the other models. Fig. 5 *a* shows the mean peak forces measured for wild-type fibrils and all six variants. The peak force observed is due to random thermal fluctuations alone (see Fig. S3) is shown as a *dashed line* for reference). Fig. 5 *b* shows the mean peak force normalized by the number of interaction interfaces interrogated during the deformations. Fig. 5 *c* shows the directional stiffness constants for each of the seven model fibrils measured for the four different SMD pulling protocols. These directional stiffness constants were obtained from the gradient of the force versus displacement plots (see Fig. S9) measured in the linear response regime and averaged over the repeat simulations.

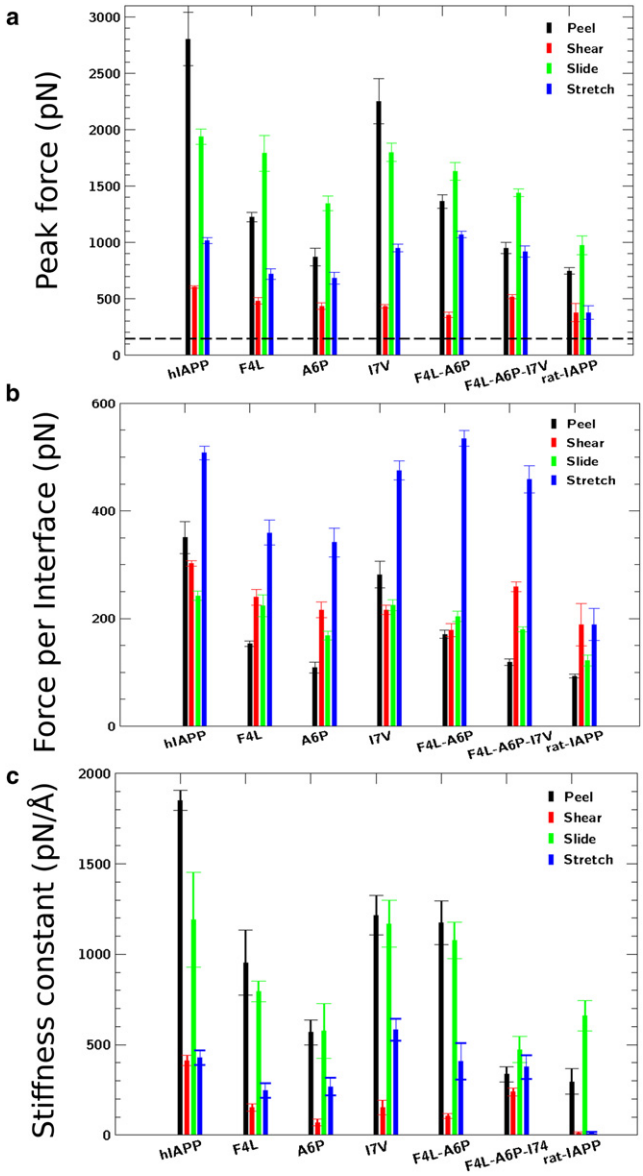


FIGURE 5 (*a*) (*Color available online only.*) Summary of the mean peak forces recorded for the seven fibril models during each type of fragmentation simulation (extracted from the data after filtering). (*Dashed line*) Maximum noise signal level. (*Error bars*) Standard error of the mean calculated from the four repeat simulations. (*b*) Normalized peak force values in terms of number of interaction interfaces disrupted during the deformation (two for stretch and shear, eight for peel and slide). (*c*) Directional stiffness constants extracted from the gradient of the force versus displacement graphs in the linear region (before exertion of the peak force).

The magnitudes of the forces measured by SMD are known to be dependent on the pulling velocity used to enforce the conformational change (44,45), as shown in Fig. S2 *b*, and as was observed from simulations detaching single peptides from A$\beta$ fibrils (21). However, because the magnitudes and durations of the forces experienced by individual fibrils during fragmentation by stirring (which has been shown to affect the cytotoxicity of fibrils (5,10)) are unknown, it is the changes in the mechanical properties of the fibril models with sequence and the mode of deformation that are most relevant, as these will apply more generally than the absolute magnitudes of the forces. Fig. 5, *a* and *b*, shows that the peak forces measured for the disordered rIAPP aggregate are the lowest for all deformations. The overall mechanical strength of each aggregate is governed by the weakest force required to induce structural failure in any direction. Using this criterion, the wild-type fibrils are the strongest, whereas the A6P and the rIAPP variants offer the least resistance to an applied force. Nevertheless, the disordered aggregates consistently have mechanical resistance above the levels of thermal noise due to the presence of van der Waals (see Table S1) and hydrogen-bonding interactions (Fig. 3 *b*) between the peptide strands.

Fig. 5, *a* and *b*, shows that the peak forces required to fragment the model fibrils depend on both the peptide sequence and the directionality of the deformation applied during the SMD. Fig. 5 *c* shows that the stiffness constants measured in the linear response regime before the application of the peak force are also sequence-dependent and anisotropic. Single molecule experiments and SMD simulations to probe the fracture forces necessary to disrupt the structure of folded proteins have previously shown that the mechanical resistance is dependent on the pulling geometry (46–48); here we show that this is also the case in SMD simulations of peptide assemblies. This is consistent with the observation that there is no direct correlation between the enthalpic stability of a model fibril and its mechanical resistance in silico, as can be seen from comparing Fig. 3 *c* and Fig. 5, *a*–*c*, because fibril fragmentation is a nonequilibrium process during the SMD calculations.

## Interatomic interactions in the fibril determine the response to mechanical stress

Fig. 5 *b* shows that all ordered fibrillar aggregates are most resistant (per interaction interface) to the stretch deformation, which directly interrogates the strength of the inter-$\beta$-sheet hydrogen bonds along the long axis of the fibril

that are primarily responsible for the general occurrence of amyloid. Comparing Fig. 5 *b* with Fig. 3 *a* shows that the mechanical resistance of fibrils to stretch is higher when there is more interstrand hydrogen bonding and the aggregate has greater $\beta$-sheet content. As the sequences of the variants were chosen to minimize differences in side-chain hydrogen-bonding interactions, the number of side-chain hydrogen bonds is similar for all variants (with the exception of rat-IAPP and A6P, Fig. 3 *b*). Consequently, the side-chain interactions play a relatively minor role in determining the sequence dependence of the mechanical resistance to stretch for this choice of variants.

Fibrils are consistently less resistant to the shear deformation than to stretch (Fig. 5, *a–c*), as shear places stress on the $\beta$-sheet hydrogen-bonding network perpendicular to the long axis of the fibril rather than along its length. This implies that the hydrogen-bonding network provides a cooperative resistance to forces applied along the fibril. The peel and slide deformations primarily address the hydrophobic core intersheet interactions within the fibrils. The peel deformation—in which the $\beta$-sheets are forced apart, thus exposing the hydrophobic core—was responsible for the two largest peak forces (2804.33 $\pm$ 237.15 pN for the wild-type and 2253.88 $\pm$ 201.26 pN for I7V) measured by the SMD simulations (Fig. 5 *a*). The relative importance of peel and slide was particularly sequence-dependent, as might be expected, because it depends on the molecular details of the packing within the hydrophobic core. Fig. S10 and Fig. S11 show a more detailed analysis of the energetic changes that produce the different force profiles in the peel and slide SMD.

## Role of Phe-Phe interactions within the hydrophobic core

Although the F4L variant has similar secondary structure content and backbone hydrogen bonds to the wild-type fibrils (Fig. 3, *a* and *b*), it records a significantly smaller mean peak force and a reduced mechanical stiffness constant (Fig. 5, *a* and *c*) in the peel simulations. The reasons for the differences in mechanical robustness of the wild-type sequence relative to the other models during the SMD simulations can be traced to intersheet Phe-Phe interactions. In the wild-type sequence, the Phe residues from opposite sheets orient themselves in such a way that they are interdigitated (Fig. 6, *a* and *b*), which confers the additional mechanical strength to the model fibrils observed in the peel calculations. In contrast, the leucine substitutions in the F4L variant are significantly further apart (17.75 $\pm$ 0.34 Å between the center of masses of Leu pairs on opposite $\beta$-sheets relative to 9.70 $\pm$ 0.14 Å for corresponding Phe pairs in the wild-type), as shown in Fig. 6 *c*. Similarly, in the I7V variant, which undergoes a shift of one $\beta$-sheet relative to the other, the Phe pairs on opposite sheets are much further apart (19.56 $\pm$ 0.63 Å) before SMD

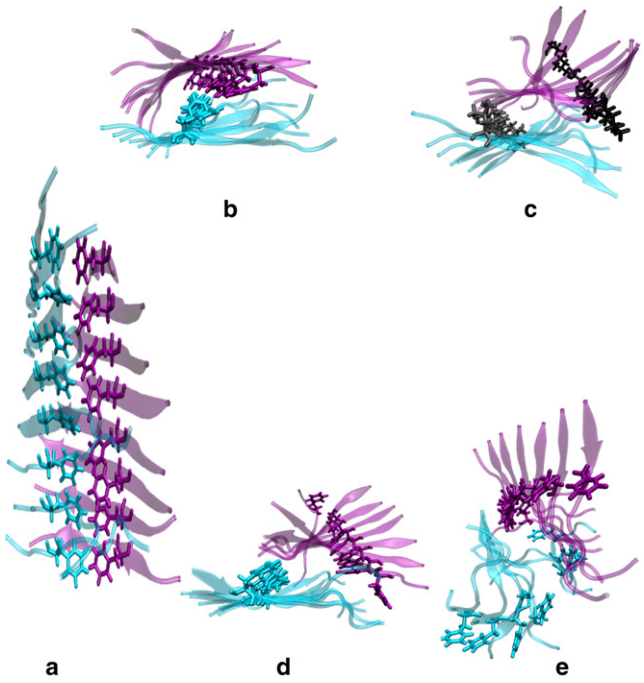


FIGURE 6 (*Color available online only.*) Orientation and alignment of Phe residues on opposing $\beta$-sheets. (*a*) Side and (*b*) top view for wild-type. Top view for (*c*) F4L (replacement Leu shown in *black* and *gray*), (*d*) I7V, and (*e*) A6P variants.

(Fig. 6 *d*). For A6P, which has reduced $\beta$-sheet content relative to the wild-type, structural disorder in the model fibril gives rise to a random orientation of the Phe residues (Fig. 6 *e*). We attribute the reduced mechanical resistance to peel observed for these variants to the absence of close-packed intersheet Phe residues in the model fibrils.

## Fibrils have weak points that reduce their mechanical resistance

All ordered fibrillar aggregates demonstrated the greatest resistance per interface to the stretch deformation, which directly interrogates the strength of the hydrogen-bonding network along the long axis of the fibril. The wild-type, I7V, F4L-A6P, and F4L-A6P-I7V fibrils display mean peak forces under stretch of ~1000 pN. However, the mean peak force for the F4L, A6P, and rIAPP variants is significantly lower (719.20 $\pm$ 46.39pN, 682.95 $\pm$ 53.65pN, and 377.79 $\pm$ 59.96pN, respectively) with correspondingly lower stiffness constants (Fig. 5 *c*). Fig. 3 *a* shows that the disruptive effect of the proline substitution in the A6P and rIAPP variants results in aggregates containing a higher proportion of disordered strands (63% and 78%, respectively, compared to only 34% for the wild-type), indicating that there are numerous positions where the chain of inter-$\beta$-sheet hydrogen-bonding interactions are interrupted (see Fig. 3 *b*).

The reduced mechanical resistance of aggregates constructed from these sequences can be explained by the

increased number of defects present in these structures. These defects act as fracture points that are the first to undergo mechanical failure under stress. The importance of these defects is emphasized by the anomalously low mean stretch force recorded for the F4L variant. Although aggregates of this sequence possess equivalent secondary structure content compared to the other structurally ordered fibrils, some of the SMD simulations performed start from an aggregate containing a defect in which a single peptide strand in a disordered conformation interrupts an otherwise ordered $\beta$-sheet (see Fig. S12). This defect acts as a weak spot in the fibril, and despite the robustness of the rest of the structure it nevertheless undergoes mechanical failure at comparatively low forces.

To test the hypothesis that the defects can be the cause of structural failure in fibrils, longer ($16 \times 2$) models of the wild-type sequence were constructed containing a defect (in the form of a disordered $\beta$-strand five strands from one end of the model fibril) as shown in Fig. S13. These were then subjected to the stretch deformation in an equivalent manner to the shorter ($8 \times 2$) fibrils. As expected, the defect acted as the fracture point in every one of the four repeat simulations. These simulations indicate that the mechanical resistance of fibrils depends not only upon peptide sequence and the relative arrangements of the individual $\beta$-strands within the fibrils, but also upon the number of flaws in the quasicrystalline peptide array. Consequently, growth conditions that decrease the number of defects—for example, if amyloid formation takes place very slowly under conditions that are close to equilibrium—result in fibrils that would be expected to be more resistant to mechanical stress than those grown so rapidly that numerous defects are annealed into their structure.

## CONCLUSIONS

We have used SMD simulations to probe the mechanical response of a series of amyloid fibril models built from peptide sequences chosen to have properties intermediate between the highly amyloidogenic human amylin fragment SNNFGAILSS and its nonamyloidogenic rat counterpart. After equilibration in the absence of an applied force, we found that the wild-type, the F4L, and I7V variants retained a high degree of $\beta$-sheet content and remained as ordered fibrillar arrays, and the A6P, F4L-A6P, and F4L-A6P-I7V variants had increased levels of disorder relative to the wild-type. We noted that the rIAPP became visibly disordered after 22 ns of MD.

Four distinct deformation protocols that applied force in different directions were used to induce mechanical failure in the fibrils, showing that the mechanical response depends on the direction of the applied force. Consequently, care must be taken when reporting quantities such as the Young's modulus of amyloid fibrils based on experimental measurements or computational data, because the results will differ depending on the precise manner in which the force is applied. All aggregates except the disordered rIAPP showed the greatest mechanical resistance per interface to the stretch deformation, which directly tests the strength of the $\beta$-sheet hydrogen-bonding interactions parallel to the long axis of the fibril. The relative strengths of all of the other interfaces varied with sequence. Whereas stretch primarily interrogates the $\beta$-sheet hydrogen-bonding network common to all fibrils, the resistance to the other deformations also rely on the molecular details of packing within the hydrophobic core.

Understanding the impact of the amino-acid sequence on the mechanical response is also likely to be of therapeutic importance. In vivo, genetic mutations may lead to the formation of mechanically less stable fibrils that are prone to fragmentation. Brittle fibrils would not only potentially increase the likelihood of early onset of amyloid-related disease through increased seeding but may also increase toxicity because the shorter fragments have been shown to disrupt cell membranes and can have enhanced cytotoxicity (5,10). Early onset type II diabetes caused by a missense mutation in the amylin gene within the Japanese population (49) results in a change of the first serine residue to a glycine residue in the hIAPP20−29 region (SNNFGAILSS becomes GNNFGAILSS). It has been reported that this amylin variant shows increased fibrillation kinetics and enhanced cytotoxicity relative to wild-type amylin (50). This particular mutation was not explicitly explored in this study, because changing a terminal residue is unlikely to influence mechanical behavior as significantly as a nonterminal mutation in the full-length protein. Nevertheless, our simulation results suggest that a plausible mechanism linking enhanced fibrillation to seeding and to cytotoxicity could be changes in the mechanical properties resulting from the sequence substitution. Future MD simulations using the full-length amylin fibrils will now be performed to test this hypothesis.

The SMD simulations also showed that increased disorder and the presence of structural defects within the fibrils consistently reduced their ability to withstand an applied force by introducing weak points prone to mechanical failure. The observation that defects are able to dominate mechanical properties is consistent with our understanding of inorganic materials, such as metals and ceramics, where the role of dislocations and point and line defects in structural failure has been extensively studied (51). It also implies that the mechanical properties of fibrils will depend on the physical conditions under which they are formed. Slow nucleation and growth that takes place close to equilibrium conditions would be expected to result in fibrils containing fewer defects than those that have grown rapidly, and would therefore produce fibrils able to resist higher mechanical stress. It has been suggested that the preferential fracture of fibrils at defect locations can give rise to a self-healing mechanism that is responsible for the high

levels of structural order present in fibrils (19), a hypothesis that is supported by our MD simulations.

Moreover, a prion strain that has a molecular structure capable of accommodating numerous defects may well be inherently more promiscuous than one formed from fibrils with a unique and high regular quasicrystalline structure, which would provide another molecular basis, in addition to seeding, for the observation that frangible prions have greater infectivity (8). Knowledge of the factors governing the mechanical performance of amyloid (and amyloidlike) fibril assemblies will be useful in the design and construction of nanomaterials (52,53) based on the self-assembly properties of amyloid for applications such as bioscaffolds, drug delivery devices (18), and nanowire templates (54). In such applications, it may even be desirable to engineer defects into self-assembling systems to produce a material that is more malleable at the macroscopic level. This could be achieved, for example, by doping with a low concentration of synthetic peptides containing one or more amino-acid substitutions incapable of forming conventional hydrogen-bonding interactions within a $\beta$-sheet, by mutating the dopant so it includes a disruptive proline residue, or by introducing a substitution designed to disrupt electrostatic interactions within the mature fibril.

This strategy for nanomaterial design has already been used in computer simulations of tubular nanostructures formed from $\beta$-helical protein motifs that have shown that substitutions with synthetic amino acids (such as 1-aminocyclopentane-1-carboxylic acid) can alter their structural stability (55). Steered molecular dynamics simulations, such as those reported here, could well prove invaluable in the bottom-up design of novel nanomaterials, as well is in the design of strategies to decrease fibril fragmentation for therapeutic use.

## SUPPORTING MATERIAL

One table and 13 figures are available at http://www.biophysj.org/biophysj/supplemental/S0006-3495(12)00036-7.

We thank David Middleton for the provision of coordinate files for the wild-type fibril template, Simon Woods for advice on data filtering techniques, and Peter Olmsted for discussions on calculating the directional stiffness constants.

This work was funded by the Engineering and Physical Sciences Research Council (UK) through the award of a doctoral training studentship to H.N. We thank the UK National Grid Service for contributing computational resources to the project.

## REFERENCES

1. Chiti, F., and C. M. Dobson. 2006. Protein misfolding, functional amyloid, and human disease. *Annu. Rev. Biochem.* 75:333–366.
2. Aguzzi, A., and T. O'Connor. 2010. Protein aggregation diseases: pathogenicity and therapeutic perspectives. *Nat. Rev. Drug Discov.* 9:237–248.
3. Walsh, D. M., I. Klyubin, …, D. J. Selkoe. 2002. Amyloid-$\beta$ oligomers: their production, toxicity and therapeutic inhibition. *Biochem. Soc. Trans.* 30:552–557.
4. Glabe, C. G. 2008. Structural classification of toxic amyloid oligomers. *J. Biol. Chem.* 283:29639–29643.
5. Lee, Y. J., R. Savtchenko, …, I. V. Baskakov. 2011. Molecular structure of amyloid fibrils controls the relationship between fibrillar size and toxicity. *PLoS ONE.* 6:e20244.
6. Martins, I. C., I. Kuperstein, …, F. Rousseau. 2008. Lipids revert inert A$\beta$ amyloid fibrils to neurotoxic protofibrils that affect learning in mice. *EMBO J.* 27:224–233.
7. Engel, M. F., L. Khemtémourian, …, J. W. Höppener. 2008. Membrane damage by human islet amyloid polypeptide through fibril growth at the membrane. *Proc. Natl. Acad. Sci. USA.* 105:6033–6038.
8. Tanaka, M., S. R. Collins, …, J. S. Weissman. 2006. The physical basis of how prion conformations determine strain phenotypes. *Nature.* 442:585–589.
9. Collins, S. R., A. Douglass, …, J. S. Weissman. 2004. Mechanism of prion propagation: amyloid growth occurs by monomer addition. *PLoS Biol.* 2:e321.
10. Xue, W.-F., A. L. Hellewell, …, S. E. Radford. 2009. Fibril fragmentation enhances amyloid cytotoxicity. *J. Biol. Chem.* 284:34272–34282.
11. Xue, W.-F., A. L. Hellewell, …, S. E. Radford. 2010. Fibril fragmentation in amyloid assembly and cytotoxicity: when size matters. *Prion.* 4:20–25.
12. Mostaert, A. S., R. Crockett, …, S. P. Jarvis. 2009. Mechanically functional amyloid fibril in the adhesive of a marine invertebrate as revealed by Raman spectroscopy and AFM. *Arch. Histol. Cytol.* 72:199–207.
13. Mostaert, A. S., M. J. Higgins, …, S. P. Jarvis. 2006. Nanoscale mechanical characterization of amyloid fibrils discovered in a natural adhesive. *J. Biol. Phys.* 32:393–401.
14. Guo, S., and B. B. Akhremitchev. 2006. Packing density and structural heterogeneity of insulin amyloid fibrils measured by AFM nanoindentation. *Biomacromolecules.* 7:1630–1636.
15. del Mercato, L. L., G. Maruccio, …, R. Rinaldi. 2008. Amyloid-like fibrils in elastin-related polypeptides: structural characterization and elastic properties. *Biomacromolecules.* 9:796–803.
16. Smith, J. F., T. P. J. Knowles, …, M. E. Welland. 2006. Characterization of the nanoscale properties of individual amyloid fibrils. *Proc. Natl. Acad. Sci. USA.* 43:15806–15811.
17. Kol, N., L. Adler-Abramovich, …, I. Rousso. 2005. Self-assembled peptide nanotubes are uniquely rigid bioinspired supramolecular structures. *Nano Lett.* 5:1343–1346.
18. Graveland-Bikker, J. F., I. A. Schaap, …, C. G. de Kruif. 2006. Structural and mechanical study of a self-assembling protein nanotube. *Nano Lett.* 6:616–621.
19. Knowles, T. P., A. W. Fitzpatrick, …, M. E. Welland. 2007. Role of intermolecular forces in defining material properties of protein nanofibrils. *Science.* 318:1900–1903.
20. Meersman, F., R. Q. Cabrera, …, V. Dmitriev. 2011. Structural and mechanical properties of TTR105-115 amyloid fibrils from compression experiments. *Biophys. J.* 100:193–197.
21. Raman, E. P., T. Takeda, …, D. K. Klimov. 2007. Mechanical unbinding of A$\beta$ peptides from amyloid fibrils. *J. Mol. Biol.* 373:785–800.
22. Paparcone, R., S. Keten, and M. J. Buehler. 2010. Atomistic simulation of nanomechanical properties of Alzheimer's A$\beta$(1-40) amyloid fibrils under compressive and tensile loading. *J. Biomech.* 43:1196–1201.
23. Paparcone, R., and M. J. Buehler. 2011. Failure of A$\beta$(1-40) amyloid fibrils under tensile loading. *Biomaterials.* 32:3367–3374.
24. Paparcone, R., M. A. Pires, and M. J. Buehler. 2010. Mutations alter the geometry and mechanical properties of Alzheimer's A$\beta$(1-40) amyloid fibrils. *Biochemistry.* 49:8967–8977.
25. Madine, J., E. Jack, …, D. A. Middleton. 2008. Structural insights into the polymorphism of amyloid-like fibrils formed by region 20-29 of

amylin revealed by solid-state NMR and x-ray fiber diffraction. *J. Am. Chem. Soc.* 130:14990–15001.

26. Westermark, P., U. Engström, …, C. Betsholtz. 1990. Islet amyloid polypeptide: pinpointing amino acid residues linked to amyloid fibril formation. *Proc. Natl. Acad. Sci. USA.* 87:5036–5040.
27. Ashburn, T. T., and P. T. Lansbury. 1993. Interspecies sequence variations affect the kinetics and thermodynamics of amyloid formation: peptide models of pancreatic amyloid. *J. Am. Chem. Soc.* 115:11012–11013.
28. Moriarty, D. F., and D. P. Raleigh. 1999. Effects of sequential proline substitutions on amyloid formation by human amylin 20–29. *Biochemistry.* 38:1811–1818.
29. Kapurniotu, A., A. Schmauder, and K. Tenidis. 2002. Structure-based design and study of non-amyloidogenic, double N-methylated IAPP amyloid core sequences as inhibitors of IAPP amyloid formation and cytotoxicity. *J. Mol. Biol.* 315:339–350.
30. Tracz, S. M., A. Abedini, …, D. P. Raleigh. 2004. Role of aromatic interactions in amyloid formation by peptides derived from human amylin. *Biochemistry.* 43:15901–15908.
31. Marek, P., A. Abedini, …, D. P. Raleigh. 2007. Aromatic interactions are not required for amyloid fibril formation by islet amyloid polypeptide but do influence the rate of fibril formation and fibril morphology. *Biochemistry.* 46:3255–3261.
32. Rivera, E., J. Straub, and D. Thirumalai. 2009. Sequence and crowding effects in the aggregation of a 10-residue fragment derived from islet amyloid polypeptide. *Biophys. J.* 96:4552–4560.
33. Mo, Y., Y. Lu, …, P. Derreumaux. 2009. Structural diversity of the soluble trimers of human amylin (20–29) peptide revealed by MD simulation. *J. Chem. Phys.* 130:125101–125106.
34. Wu, C., H. Lei, and Y. Duan. 2004. Formation of partially ordered oligomers of amyloidogenic hexapeptide (NFGAIL) in aqueous solution observed in MD simulation. *Biophys. J.* 87:3000–3009.
35. Zanuy, D., B. Ma, and R. Nussinov. 2003. Short peptide amyloid organization: stabilities and conformations of the islet amyloid peptide NFGAIL. *Biophys. J.* 84:1884–1894.
36. Macke, T., and D. A. Case. 1998. Modeling unusual nucleic acid structures. *In* Molecular Modeling of Nucleic Acids. N. B. Leontes and J. SantaLucia, Jr., editors.; American Chemical Society, Washington, DC. 379–393.
37. Case, D. A., T. E. Cheatham, 3rd, …, R. J. Woods. 2005. The AMBER biomolecular simulation programs. *J. Comput. Chem.* 26:1668–1688.
38. Phillips, J. C., R. Braun, …, K. Schulten. 2005. Scalable molecular dynamics with NAMD. *J. Comput. Chem.* 26:1781–1802.
39. Hornak, V., R. Abel, …, C. Simmerling. 2006. Comparison of multiple AMBER force fields and development of improved protein backbone parameters. *Proteins.* 65:712–725.
40. MacKerell, Jr., A. D., …, D. Bashford, M. Karplus. 1998. All-atom empirical potential for molecular modeling and dynamics studies of proteins. *J. Phys. Chem. B.* 102:3586–3616.
41. Jorgensen, W. L., J. Chandrasekhar, …, M. L. Klein. 1983. Comparison of simple potential functions for simulating liquid water. *J. Chem. Phys.* 79:926–935.
42. Kabsch, W., and C. Sander. 1983. Dictionary of protein secondary structure: pattern recognition of hydrogen-bonded and geometrical features. *Biopolymers.* 22:2577–2637.
43. Humphrey, W., A. Dalke, and K. Schulten. 1996. VMD: visual molecular dynamics. *J. Mol. Graph.* 14:33–38, 27–28.
44. Isralewitz, B., J. Baudry, …, K. Schulten. 2001. Steered molecular dynamics investigations of protein function. *J. Mol. Graph. Model.* 19:13–25.
45. Isralewitz, B., M. Gao, and K. Schulten. 2001. Steered molecular dynamics and mechanical functions of proteins. *Curr. Opin. Struct. Biol.* 11:224–230.
46. Dietz, H., F. Berkemeier, …, M. Rief. 2006. Anisotropic deformation response of single protein molecules. *Proc. Natl. Acad. Sci. USA.* 103:12724–12728.
47. Brockwell, D. J., E. Paci, …, S. E. Radford. 2003. Pulling geometry defines the mechanical resistance of a $\beta$-sheet protein. *Nat. Struct. Biol.* 10:731–737.
48. Carrion-Vazquez, M., H. Li, …, J. M. Fernandez. 2003. The mechanical stability of ubiquitin is linkage dependent. *Nat. Struct. Biol.* 10:738–743.
49. Sakagashira, S., T. Sanke, …, K. Nanjo. 1996. Mis-sense mutation of amylin gene (S20G) in Japanese NIDDM patients. *Diabetes.* 5:1279–1281.
50. Sakagashira, S., H. J. Hiddinga, …, N. L. Eberhardt. 2000. S20G mutant amylin exhibits increased in vitro amyloidogenicity and increased intracellular cytotoxicity compared to wild-type amylin. *Am. J. Pathol.* 157:2101–2109.
51. Stoneham, A. M. 1975. Theory of defects in solids: electronic structure of defects in insulators and semiconductors. *In* Monograph on the Physics and Chemistry of Materials..; Oxford University Press, Cambridge, UK. 159–186.
52. Cherny, I., and E. Gazit. 2008. Amyloids: not only pathological agents but also ordered nanomaterials. *Angew. Chem. Int. Ed. Engl.* 47:4062–4069.
53. Gras, S. L. 2007. Amyloid fibrils: from disease to design. New biomaterial applications for self-assembling cross-$\beta$ fibrils. *Aust. J. Chem.* 60:333–342.
54. Scheibel, T., R. Parthasarathy, …, S. L. Lindquist. 2003. Conducting nanowires built by controlled self-assembly of amyloid fibers and selective metal deposition. *Proc. Natl. Acad. Sci. USA.* 100:4527–4532.
55. Zanuy, D., F. Rodríguez-Ropero, …, C. Aleman. 2007. Stability of tubular structures based on $\beta$-helical proteins: self-assembled versus polymerized nanoconstructs and wild-type versus mutated sequences. *Biomacromolecules.* 8:3135–3146.